ORIGINAL PAPER

Detailed study on MOCVD of wafer-scale MoS$_2$ monolayers: From nucleation to coalescence

Songyao Tang[1] · Annika Grundmann[1] · Hleb Fiadziushkin[1] · Amir Ghiami[1] · Michael Heuken[1,2] · Andrei Vescan[1] · Holger Kalisch[1]

Abstract

Metal–organic chemical vapour deposition (MOCVD) has become one of the most promising techniques for the large-scale fabrication of 2D transition metal dichalcogenide (TMDC) materials. Despite efforts devoted to the development of MOCVD for TMDC monolayers, the whole picture of the growth process has not been fully unveiled yet. In this work, we employ a commercial AIXTRON CCS MOCVD tool for the deposition of MoS$_2$ on sapphire using standard precursors and H$_2$ as carrier gas. Adsorption and diffusion of Mo adatoms on the substrate are found to be decisive for nucleation. By lowering temperature from 650 to 450 °C, a uniform distribution of nuclei on sapphire terraces is achieved. Full coalescence of MoS$_2$ monolayers with limited bilayer formation (~ 15%) is then realized at 700 °C. This study highlights the importance of understanding the details of film formation mechanisms and developing multi-stage MOCVD processes for 2D TMDC films.

Introduction

Although research activities in the field of 2D TMDC are expanding rapidly, the industrialization of 2D devices is still handicapped by the lack of a dedicated production technology for reproducible and uniform TMDC thin films on wafer scale. With MOCVD being a promising candidate, considerable progress has been made in optimizing deposition processes [1, 2]. A typical MOCVD process consists of the following fundamental mechanisms: decomposition of precursors, mass transport from gas phase to substrate, adsorption and diffusion of adatoms on substrate, nucleation/growth as well as desorption of adatoms from the substrate. Supersaturation of growth species on the substrate is the central requirement to create non-equilibrium conditions leading to film formation. The complexity of both thermodynamic and kinetic factors involved makes it difficult to consider all mechanisms in one discussion [3]. Despite some valuable theoretical modelling and calculation results [4–7], it is still challenging to identify the impact of multiple

factors and conditions during development and optimization of growth processes. Up to now, a large number of process details and growth parameters have been reported to influence the final output of MOCVD processes, including substrate pre-treatment [8–11], growth temperature [12–14], selection and mass flow rate of precursors [13, 15–20]. To complicate things further, strongly different reactor geometries from horizontal [14] and vertical [17] flow, multi-wafer planetary [8, 12, 15] to showerhead [16, 19, 20] obviously lead to in part fundamentally contradictory findings, e.g. concerning the selection of carrier gas of either N$_2$ or H$_2$. The causality behind this apparently chaotic situation is that any variation of individual growth parameters or conditions will impact several sub-processes — e.g. distance and temperature distribution of the flow path from inlet to substrate could severely affect decomposition and pre-reactions of precursors, adsorption/desorption, diffusion of adatoms and nucleation/growth, resulting in strong variations of processes and epilayer formed. Here, we report on the systematic development of a two-stage MOCVD process to prepare MoS$_2$ monolayers on 2″ sapphire substrates using the AIXTRON CCS (close-coupled showerhead) MOCVD platform equipped with state-of-the-art in situ monitoring. Nucleation at different temperatures is comprehensively analysed to clarify the correlation between adsorption and diffusion of the growth-limiting Mo adatoms on the substrate. Details of the mechanisms from nucleation to film coalescence are

✉ Songyao Tang
tang@cst.rwth-aachen.de

1 Compound Semiconductor Technology, RWTH Aachen University, Sommerfeldstr. 18, 52074 Aachen, Germany

2 AIXTRON SE, Dornkaulstr. 2, 52134 Herzogenrath, Germany

studied, supported by in situ measurements as well as a thorough ex situ sample characterization after different stages of growth. With our optimized two-stage MOCVD process, a fully-coalesced MoS$_2$ monolayer can be fabricated in 75 min with sparse bilayer (BL) nucleation (~15%). Quality and properties of the MoS$_2$ monolayers with different values of coverage are evaluated by Raman and photoluminescence (PL) spectroscopy.

Experimental details

All MOCVD processes were carried out in an AIXTRON CCS reactor (7×2″ configuration) with ARGUS temperature homogeneity control and LayTec in situ monitoring, which enables a real-time measurement of spectral reflectance and emissivity-corrected true temperature. In the following, all mentioned temperatures refer to the true temperature on the substrate surface. 2″ c-plane sapphire with a nominal 0.2° off-cut towards m-plane is used as substrate. Molybdenum hexacarbonyl (MCO, 99.9%) and di-tert-butyl sulphide (DTBS, 99.999%) are used as precursors for Mo and S, respectively. All processes start with a standard desorption procedure under 150 hPa H$_2$ atmosphere at 1050 °C for 30 min [8]. The nucleation and lateral-growth stages are also performed under pure H$_2$ atmosphere at 20 hPa total pressure. The molar flow of MCO is chosen as ~28 nmol/min and that of DTBS ~180 μmol/min (S:Mo ratio of ~6400). After H$_2$ desorption, the temperature is immediately ramped down and then stabilized for 10 min. During these 10 min, the fluxes of carrier gas (H$_2$) through the source containers are also stabilized. Different temperatures between 650 °C and 450 °C and varied nucleation durations from 15 to 75 min were tested to study the affinity of adatoms to form stable nuclei and to optimize the nucleation morphology. After an optimized nucleation process (stage I) with a temperature of 450 °C and duration of 30 min, the temperature is linearly ramped up to 700 °C in 15 min (w/o growth interruption)

and kept constant for certain periods of time (lateral-growth stage II). Here, different durations of stage II from 15 to 45 min (including the first 15 min for temperature ramp-up) are also compared to trace how the monolayer is coalescing step by step. Samples are analysed by in situ reflectance transients, scanning electron microscopy (SEM), atomic force microscopy (AFM) as well as Raman and PL spectroscopy.

Results and discussion

As a starting point, 650 °C was used for the nucleation of MoS$_2$. The resulting nucleation morphology after 15 min and 30 min is shown in Fig. 1a and b, respectively. It is clearly visible that the adatoms preferentially accumulate along certain orientations which are roughly perpendicular to the sapphire flat. The intentional substrate off-cut is towards m-plane (perpendicular to the a-plane flat) and therefore these lines are obviously correlated to atomic steps on the sapphire surface [10, 11]. As nucleation proceeds (from 15 to 30 min), these oriented nano-nuclei will merge and form chains. Strikingly, the regions between the MoS$_2$ chains remain mostly uncovered with only a couple of nuclei occasionally appearing. This can be interpreted as the sapphire steps being thermodynamically favourable nucleation sites for MoS$_2$ [21, 22], whilst the Mo diffusion length on sapphire terraces is larger than their typical size.

When extending the nucleation stage under the same conditions for another 45 min, as shown in Fig. 1c and d, it can be recognized that the chains mainly grow in vertical direction forming BLs. The lateral dimension of these chains barely increases during these 45 min. Instead, additional nucleation takes place on some terraces with relatively large area, forming typical triangular monolayer domains. Based on the above observations, the following hypotheses can be drawn to explain the mechanisms involved in this stage: (i) due to the high diffusivity of Mo adatoms at 650 °C, all adatoms can diffuse for a long distance. The
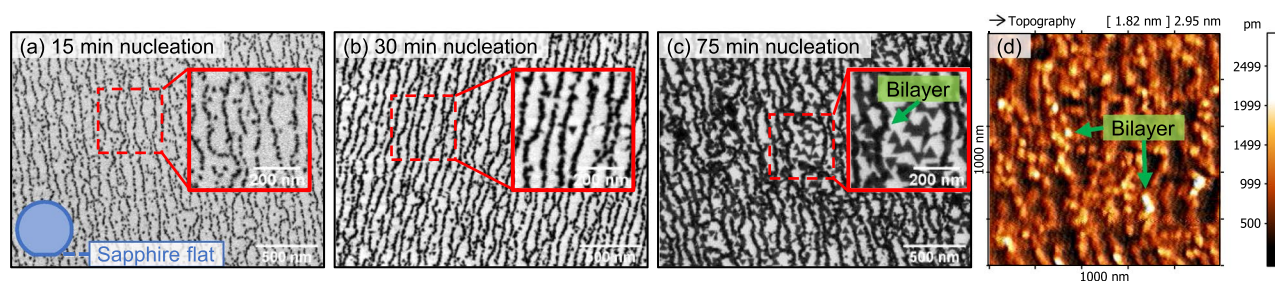
Fig. 1 Evolution of MoS$_2$ morphology after 15 min (a), 30 min (b), and 75 min (c) nucleation at 650 °C. The lower left inset in (a) indicates the alignment of the sapphire flat (a-plane) for all SEM measurements here. Red boxes are zoomed-in images of corresponding regions. Bilayer (BL) nucleation chains present a slightly deeper SEM contrast than monolayers in (c). (d) AFM of MoS$_2$ after 75-min nucleation, green arrows indicate BL nucleation

lower limit for the diffusion length is approximately 70 nm, given by the average distance between the sapphire steps seen in Fig. 1. The Mo adatoms diffuse on the substrate until they attach to the atomic sapphire steps which are energetically favourable for nucleation. This results in the nucleation chains along the steps of the sapphire substrate. (ii) After the MoS$_2$ chains fully cover the steps on the sapphire surface, the high diffusivity of adatoms makes it favourable to climb onto the chains of monolayer MoS$_2$, triggering BL growth [14]. From the perspective of growth thermodynamics, the top surface of monolayer MoS$_2$ may act as the more favourable nucleation site than the atomically smooth sapphire terraces. (iii) On certain large area terraces, since the distance between two sapphire steps is relatively high (e.g. in the inset of Fig. 1c, here the terrace is more than 200 nm wide), some adatoms could either fail to reach a sapphire step or they could be confined by the super steps to BL chains ("super" means too high for adatoms to surmount). As a result, some adatoms could nucleate stable triangular domains on terraces.

Based on these hypotheses, the high diffusivity of adatoms at 650 °C is accused of not only premature BL growth, but also the inhomogeneous distribution of nuclei on the sapphire substrate. To reduce Mo adatom diffusivity, lower nucleation temperatures, namely 550 °C and 450 °C, have been studied. The obtained morphology after 30 min can be compared in Fig. 2a to c. As expected, the number of nano-nuclei located on individual terraces increases with decreased temperature. Such a homogeneous nucleation density as shown in Fig. 2c is required for controlled monolayer coalescence.

After 30-min nucleation at 450 °C, a relatively uniform nucleation on sapphire steps and terraces is achieved with approximately 55% coverage. However, extended growth under these conditions might result in continued nucleation on top of already-deposited monolayer domains or eventually on the sapphire terraces, similar to the case at 650 °C shown in Fig. 1. This continued nucleation competes with lateral growth, leading to chaotic and uncontrollable 3D growth rather than to monolayer coalescence.

Therefore, for the lateral-growth stage, the temperature is raised up to 700 °C over 15 min and held constant for different periods of time. The total duration of the lateral-growth stage varies from 15 to 45 min, and the in situ reflectance measured at 405 nm as well as the true temperature for different processes are compared in Fig. 3a. It should be noted that in all processes, in situ reflectance transients allow for a direct real-time monitoring of material deposition with an approximately linear dependence between the transient reflectance slope and the deposition rate. The slope at the very beginning of nucleation (e.g. from 0 to 10 min) is found to be slightly smaller than that near the end of nucleation (e.g. from 20 to 30 min), which may imply the difference between the formation of initial nuclei and the growth of previously formed nuclei. In the lateral-growth stage, the slope remains almost constant as long as growth conditions are constant. (The change in slope between 30 and 45 min is due to the temperature ramp and not considered here.) Close to monolayer coalescence (60 to 75 min), the slope is slightly decreasing, attributed to a reduced density of domain edges available for lateral growth. The described process is highly reproducible and repeatable as shown by the overlapping in situ reflectance curves recorded for the different processes under identical process conditions (except growth time).

The development of MoS$_2$ morphology/topography is recorded via SEM and AFM. In SEM images in Fig. 3b, it can be clearly seen that the nano-nuclei gradually expand and merge with each other. After 75-min total growth time, a fully-coalesced MoS$_2$ monolayer is successfully produced. AFM topography scans recorded for the same samples (not shown here) are in good agreement with SEM.

However, some abnormal tiny bright sticks on monolayer surfaces with a strong SEM contrast (marked by green arrows in Fig. 3b) can be observed after coalescence. Judging from a slight increase in roughness under AFM, these could be vertical nanosheets (≤ 1 nm) resulting from the fast
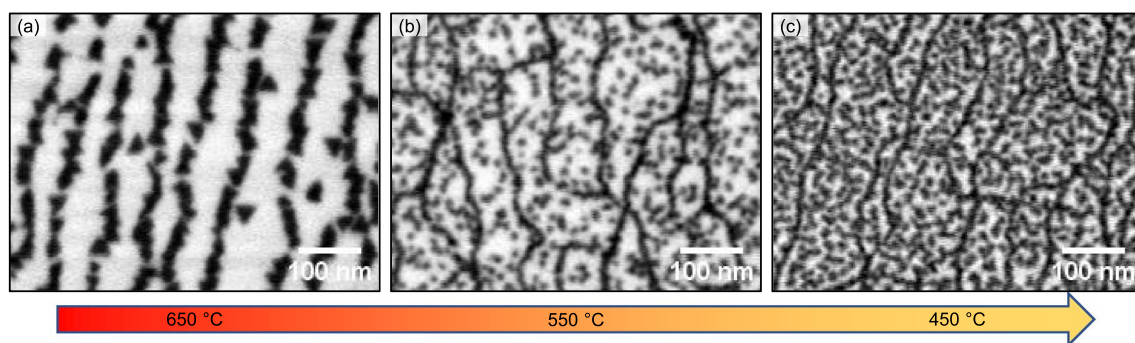
Fig. 2 Comparison of MoS$_2$ nucleation for 30 min at different temperatures. The number of nuclei on terraces greatly increases as the temperature decreases

(a)

(b)
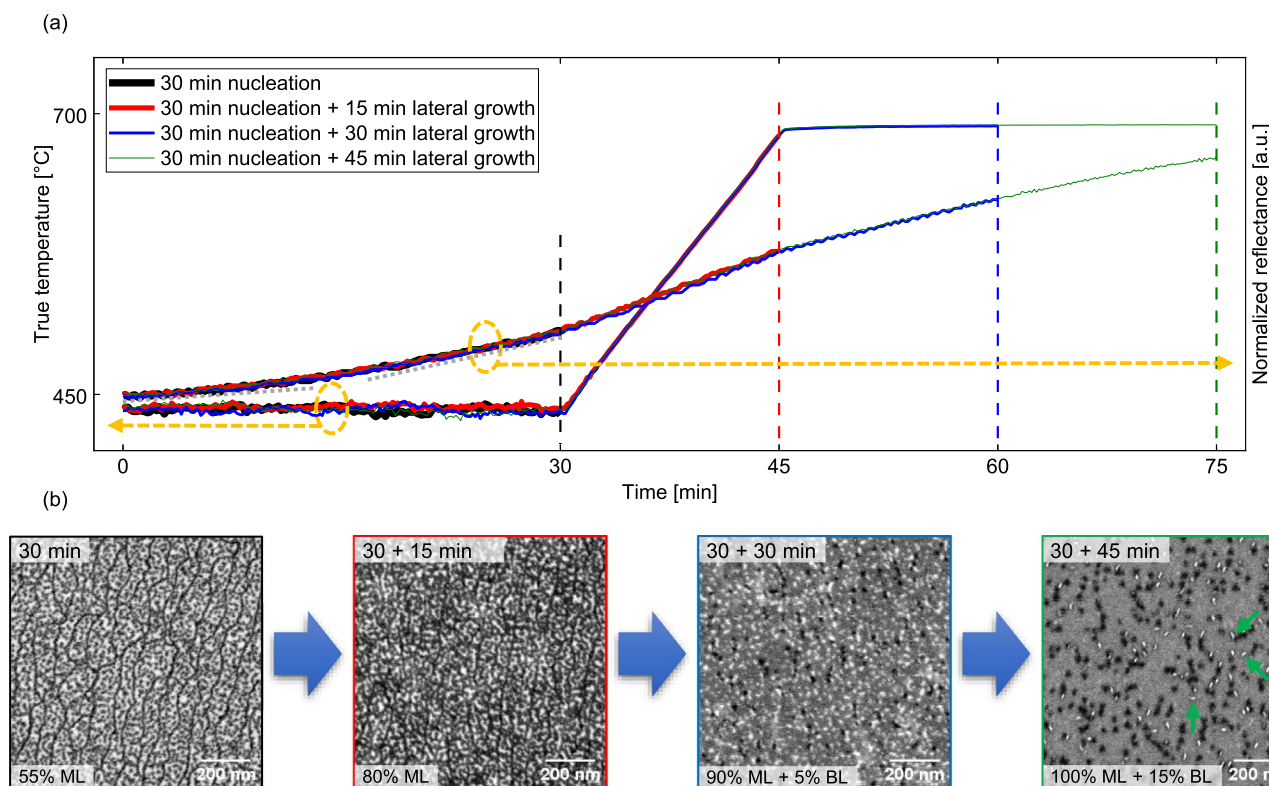
Fig. 3 **a** In situ transients measured during four different processes. Left axis is the true temperature. Right axis is the reflectance at 405 nm after normalization. Vertical-dashed lines indicate the end points of individual processes. Grey-dotted lines are guide for eyes to show the slope variations. **b** Evolution of MoS_2 monolayer from nucleation to full coalescence recorded by SEM. The corresponding monolayer (ML) and bilayer (BL) coverages are calculated via ImageJ [23] and given in the SEM images. Green arrows in the rightmost image in (**b**) point at the suspected vertical nanosheets

stitching of domains and extrusion of monolayers into the normal direction of substrate as quite often observed during extended growth experiments and also reported in [24].

Raman and PL spectra of MoS_2 at different growth stages are displayed in Fig. 4a and b, respectively. In Fig. 4a, Raman peaks belonging to MoS_2 and sapphire can be evidently distinguished for all MoS_2 samples and are marked accordingly. The intensity ratio between the characteristic MoS_2 peaks (E^1_{2g} and A_{1g}) and that of the sapphire peak (near 420 cm^{-1}) is found increased with monolayer coverage rising. In the final coalesced MoS_2 monolayer film, the peak distance between the E^1_{2g} and A_{1g} mode is calculated to be 19.5 cm^{-1} after Lorentzian fitting, confirming the monolayer nature of our sample [25]. For the spectra in Fig. 4b, it is found that the PL emission intensity increases as the monolayer coverage rises. As the coverage grows from 80 to 90%, a red shift of the A exciton is observed, which can be explained by the strain generated in MoS_2 monolayers when domains merge with each other [26]. On the other hand, the spectrum of fully-coalesced MoS_2 is broadened in comparison with that of 90%-coverage MoS_2. The broadening of PL is attributed to the increment of BL contribution,

since emission energies for monolayer and bilayer MoS_2 differ [27]. Further studies have to be performed to analyse the PL spectra in more details.

Conclusion

In this work, the fundamental mechanisms of MOCVD of coalesced MoS_2 monolayers are discussed with detailed characterization during various stages of growth. Different nucleation temperatures are compared to reveal the influence of adatom diffusion/adsorption and substrate topography. A series of hypotheses considering both kinetic and thermodynamic factors are proposed to explain the evolution of nucleation morphology, which is instructive for modifying growth parameters. Based on the comprehensive understanding of MoS_2 growth, a low nucleation temperature (450 °C) is chosen. In the lateral-growth stage, coalescence of the MoS_2 monolayer is realized at a high temperature (700 °C) with sparse parasitic BL formation. It is expected that gradually ramping down the MCO supply towards coalescence (starting at around 85% coverage) might further reduce BL

Fig. 4 **a** Raman spectra measured from bare sapphire substrate and MoS$_2$ samples at different growth stages. **b** PL spectra measured from different positions on individual MoS$_2$ monolayers near coalescence with different degrees of coverage
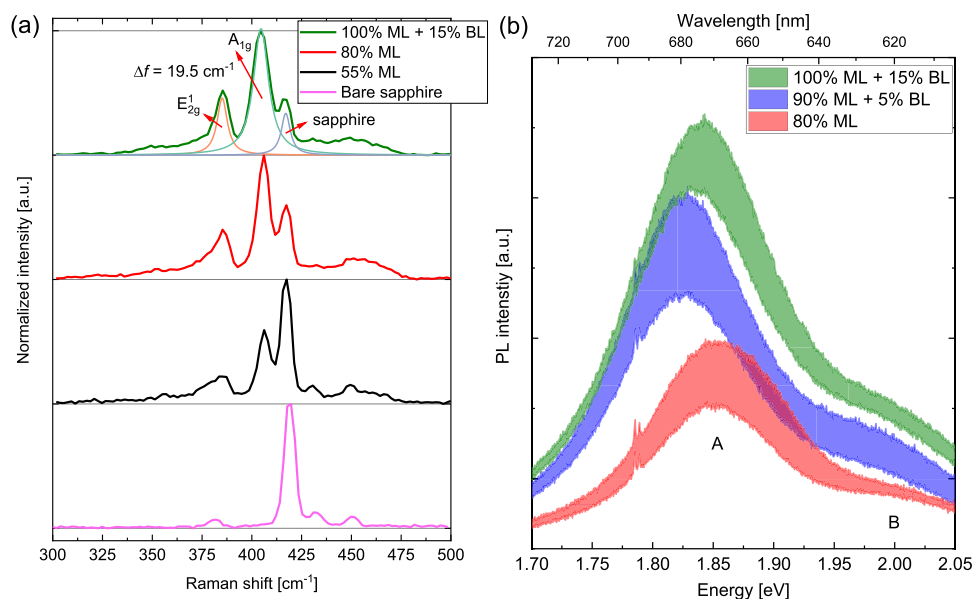
nucleation as well as the formation of vertical nanosheets. The two-stage MOCVD process reported here is a straightforward approach which could be constructive for the establishment of an industrially applicable production protocol for MoS$_2$ monolayers. The discussion about its detailed mechanisms delivers insights into the complicated interplay of various fundamental processes involved in MOCVD of 2D TMDC.

Data availability The data generated during the current study are available from the corresponding author on reasonable request.

Declarations

Conflict of interest On behalf of all authors, the corresponding author states that there is no conflict of interest.

References

1. D.H. Lee, Y. Sim, J. Wang, S.-Y. Kwon, APL Mater. **8**, 030901 (2020)
2. Q. Wang, R. Shi, Y. Zhao, R. Huang, Z. Wang, A. Amini, C. Cheng, Nanoscale Adv. **3**, 3430 (2021)
3. Y. Jung, E. Ji, A. Capasso, G.-H. Lee, J. Korean Ceram. Soc. **56**, 24 (2019)
4. S.-L. Shang, G. Lindwall, Y. Wang, J.M. Redwing, T. Anderson, Z.-K. Liu, Nano Lett. **16**, 5742 (2016)
5. H. Ye, J. Zhou, D. Er, C.C. Price, Z. Yu, Y. Liu, J. Lowengrub, J. Lou, Z. Liu, V.B. Shenoy, ACS Nano **11**, 12780 (2017)
6. Y. Nie, C. Liang, P.R. Cha, L. Colombo, R.M. Wallace, K. Cho, Sci. Rep. **7**, 1 (2017)
7. B. Pan, K. Zhang, C. Ding, Z. Wu, Q. Fan, T. Luo, L. Zhang, C. Zou, S. Huang, ACS Appl. Mater. Interfaces **12**, 35337 (2020)
8. M. Marx, A. Grundmann, Y.R. Lin, D. Andrzejewski, T. Kümmell, G. Bacher, M. Heuken, H. Kalisch, A. Vescan, J. Electron. Mater. **47**, 910 (2018)
9. W. Mortelmans, S. El Kazzi, A. Nalin Mehta, D. Vanhaeren, T. Conard, J. Meersschaut, T. Nuytten, S. De Gendt, M. Heyns, C. Merckling, Nanotechnology **30**, 465601 (2019)
10. Y. Shi, B. Groven, J. Serron, X. Wu, A. Nalin Mehta, A. Minj, S. Sergeant, H. Han, I. Asselberghs, D. Lin, S. Brems, C. Huyghebaert, P. Morin, I. Radu, M. Caymax, ACS Nano **15**, 9482 (2021)
11. M. Chubarov, T.H. Choudhury, D.R. Hickey, S. Bachu, T. Zhang, A. Sebastian, A. Bansal, H. Zhu, N. Trainor, S. Das, M. Terrones, N. Alem, J.M. Redwing, ACS Nano **15**, 2532 (2021)
12. M. Marx, S. Nordmann, J. Knoch, C. Franzen, C. Stampfer, D. Andrzejewski, T. Kümmell, G. Bacher, M. Heuken, H. Kalisch, A. Vescan, J. Cryst. Growth **464**, 100 (2017)
13. S.M. Eichfeld, L. Hossain, Y. Lin, A.F. Piasecki, B. Kupp, A.G. Birdwell, R.A. Burke, N. Lu, X. Peng, J. Li, A. Azcatl, S. McDonnell, R.M. Wallace, M.J. Kim, T.S. Mayer, J.M. Redwing, J.A. Robinson, ACS Nano **9**, 2080 (2015)
14. W. Hong, C. Park, G.W. Shim, S.Y. Yang, S.-Y. Choi, A.C.S. Appl. Mater. Interfaces **13**, 50497 (2021)
15. A. Grundmann, D. Andrzejewski, T. Kümmell, G. Bacher, M. Heuken, H. Kalisch, A. Vescan, MRS Adv. **4**, e1 (2019)

16. J. Choi, M. Ha, J.C. Park, T.J. Park, W. Kim, M. Lee, J. Ahn, Adv. Mater. Interfaces **9**, 2101785 (2022)

17. C.M. Schaefer, J.M. Caicedo Roque, G. Sauthier, J. Bousquet, C. Hébert, J.R. Sperling, A. Pérez-Tomás, J. Santiso, E. del Corro, J.A. Garrido, Chem. Mater. **33**, 4474 (2021)

18. X. Zhang, T.H. Choudhury, M. Chubarov, Y. Xiang, B. Jariwala, F. Zhang, N. Alem, G.-C. Wang, J.A. Robinson, J.M. Redwing, Nano Lett. **18**, 1049 (2018)

19. M. Seol, M. Lee, H. Kim, K.W. Shin, Y. Cho, I. Jeon, M. Jeong, H. Lee, J. Park, H. Shin, Adv. Mater. **32**, 2003542 (2020)

20. J. Mun, Y. Kim, I.S. Kang, S.K. Lim, S.J. Lee, J.W. Kim, H.M. Park, T. Kim, S.W. Kang, Sci. Rep. **6**, 1 (2016)

21. L. Chen, B. Liu, M. Ge, Y. Ma, A.N. Abbas, C. Zhou, ACS Nano **9**, 8368 (2015)

22. T. Li, W. Guo, L. Ma, W. Li, Z. Yu, Z. Han, S. Gao, L. Liu, D. Fan, Z. Wang, Y. Yang, W. Lin, Z. Luo, X. Chen, N. Dai, X. Tu, D. Pan, Y. Yao, P. Wang, Y. Nie, J. Wang, Y. Shi, X. Wang, Nat. Nanotechnol. **16**, 1201 (2021)

23. J.N. Kapur, P.K. Sahoo, A.K.C. Wong, Comput. Vis. Graph. Image Process. **29**, 273 (1985)

24. H. Li, H. Wu, S. Yuan, H. Qian, Sci. Rep. **6**, 1 (2016)

25. H. Li, Q. Zhang, C.C.R. Yap, B.K. Tay, T.H.T. Edwin, A. Olivier, D. Baillargeat, Adv. Funct. Mater. **22**, 1385 (2012)

26. H.J. Conley, B. Wang, J.I. Ziegler, R.F. Haglund, S.T. Pantelides, K.I. Bolotin, Nano Lett. **13**, 3626 (2013)

27. K.F. Mak, C. Lee, J. Hone, J. Shan, T.F. Heinz, Phys. Rev. Lett. **105**, 2 (2010)